Digital printing of shape-morphing natural materials

Ze Zhao[a], Jatin Kumar[b], Youngkyu Hwang[a], Jingyu Deng[a], Mohammed Shahrudin Bin Ibrahim[a], Changjin Huang[b,c], Subra Suresh[a,1], and Nam-Joon Cho[a,1]

[a]School of Materials Science and Engineering, Nanyang Technological University, Singapore 639798, Republic of Singapore; [b]School of Mechanical and Aerospace Engineering, Nanyang Technological University, Singapore 639798, Republic of Singapore; and [c]School of Chemical and Biomedical Engineering, Nanyang Technological University, Singapore 637459, Republic of Singapore

Contributed by Subra Suresh, August 29, 2021 (sent for review July 26, 2021; reviewed by Yonggang Huang and Guruswami Ravichandran)

We demonstrate how programmable shape evolution and deformation can be induced in plant-based natural materials through standard digital printing technologies. With nonallergenic pollen paper as the substrate material, we show how specific geometrical features and architectures can be custom designed through digital printing of patterns to modulate hygrophobicity, geometry, and complex shapes. These autonomously hygromorphing configurations can be "frozen" by postprocessing coatings to meet the needs of a wide spectrum of uses and applications. Through computational simulations involving the finite element method and accompanying experiments, we develop quantitative insights and a general framework for creating complex shapes in eco-friendly natural materials with potential sustainable applications for scalable manufacturing.

natural materials | pollen | digital printing | hygromorphing | sustainability

Materials capable of autonomously undergoing reversible changes in shape in response to environmental stimuli are subjects of rapidly growing scientific studies for possible applications in fields as diverse as clean energy harvesting (1, 2), soft robotics (3–5), sensors (6, 7), and flexible electronics (8–10). Most of the shape-morphing materials, particularly many micromaterials and nanomaterials, however, rely on nonrenewable fossil resources (3, 4, 11, 12), which could lead to potential resource shortage (13), environmental damage (14), and health risk (15–17). As an alternative pathway to pursue green chemistry and environmental sustainability, materials derived from nature are increasingly being explored for shape-morphing systems that respond to environmental stimuli. For example, controlled humidity changes lead to significant alterations in mechanical deformability and shapes of some biomaterials, including cellulose (18–22), agarose (2, 23), silk (24–26), and bacteria (27–29). However, such biomaterials are mostly extracted, synthesized, and processed exclusively from raw biomass. They often suffer from limitations in their propensity for shape transformation in response to such stimuli as moisture (1, 30) and in their scalability and cost competitiveness for large-volume applications. Attempts have been made to circumvent these limitations by incorporating mechanical constraints into a soft hygroexpandable matrix, by recourse to which preprogrammable motility can be achieved (31–33). Several techniques, such as external electric fields (34), photolithography (11, 35), molding (3, 31, 36), and microstamping (4), have been used to pattern the active and inactive components that respond to stimuli to realize complex dynamic deformation. However, heavy dependence on strict reaction control, and the requirement of elaborate processing equipment and prefabricated templates, hinder further development and potential deployment of available routes to eco-friendly shape-morphing materials. As a result, there exists a critical need to develop processes for large-scale engineering production of natural biomaterials through simple and agile manufacturing methods that are amenable to digitization. Such digital manufacturing pathways are essential for the fabrication of eco-friendly engineering components for sustainable applications.

This work demonstrates unique possibilities for producing autonomous, on-demand deformation and designing complex shapes using natural plant-based materials and readily available digital printing technologies. We begin with the example of a bilayer material to illustrate the mechanistic origins of shape evolution. This bilayer film material is engineered with moisture-active and moisture-inactive constituent layers, whose humidity-induced strain mismatch induces macroscopic deformation. The active layer is made of pliable hollow particles processed from natural plant pollen grains. This step makes use of our recent discovery of how hard pollen can be transformed into nonallergenic, soft microgels through a process analogous to simple soapmaking (37). It further exploits our recent development of a pollen-based natural material capable of autonomous actuation in response to changes in humidity (38). The innovation reported in the present work entails introducing an inactive layer (comprising styrene acrylate copolymer from standard laser toner or any natural material, such as "edible ink") which is digitally printed into custom-designed patterns on the active pollen layer. The printed layer tightly binds to the pollen paper's surface, thereby ensuring the mechanical integrity of the interface between them. This feature enables us to develop a simple and efficient way of producing a moisture-sensitive biomaterial-based system that can morph reversibly on demand into desired geometrical configurations to produce complex shapes that can be digitally custom designed and printed.

The humidity-sensitive hygromorphing behavior of the bilayer can be "frozen" through postprocessing coatings so that no

Significance

Most shape-morphing materials rely on nonrenewable fossil resources or finely extracted biomaterials, which need strict reaction control, elaborate processing equipment, or prefabricated templates to achieve controllable transformation. To circumvent these challenges, we developed an eco-friendly and scalable strategy for programmable shape evolution that integrates easy-to-process pollen biomass with cost-effective digital printing. Using this approach, specific geometrical features and architectures were customized to build complex materials with user-defined, shape-morphing abilities. These fabrication efforts were complemented by computational simulations to build quantitative and mechanistic insights into the biomaterial's characteristics for creating complex shapes with methods that are suitable for scalable manufacturing.

Author contributions: Z.Z., J.K., C.H., S.S., and N.-J.C. designed research; Z.Z., J.K., Y.H., J.D., M.S.B.I., and C.H. performed research; Z.Z., J.K., C.H., S.S., and N.-J.C. analyzed data; and Z.Z., J.K., C.H., S.S., and N.-J.C. wrote the paper.

Reviewers: Y.H., Northwestern University; and G.R., California Institute of Technology.

Competing interest statement: Z.Z., S.S., and N.-J.C. are listed as coinventors on a technology disclosure that was filed in relation to the findings of this study.

[1]To whom correspondence may be addressed. Email: SSuresh@ntu.edu.sg or NJCho@ntu.edu.sg.

This article contains supporting information online at https://www.pnas.org/lookup/suppl/doi:10.1073/pnas.2113715118/-/DCSupplemental.

Published October 18, 2021.

further shape changes occur in service. In this way, the fabricated material can be used in many applications where humidity changes occur during use of the material, thereby facilitating a wide variety of high-volume commercial applications for this technology. We further show how complex shapes as well as on-demand tilting and folding mechanisms can be produced using natural materials and geometric designs, without the need for special hinges or fasteners. The various processing steps outlined in this work are also potentially scalable for large-volume production, and we briefly summarize pathways to achieve such scalability.

With biomimetic inspiration from the hygroresponsive coiling behavior of the *Pelargonium* plant species' awn that depends on cellulose microfibrils with tilted alignment (39), we designed and digitally printed the inactive toner layer into stripe patterns of various orientations and precisely controlled the coiling morphology of the bilayer. Furthermore, the toner coverage rate and relative humidity (RH) levels provide additional flexibility in tuning the degree of shape change. We also performed detailed computational simulations using the finite element method (FEM) to model and quantitatively predict the shape and geometry of deformation in response to humidity. These simulations provide quantitative details and mechanistic insights into the material's performance characteristics that cannot be obtained solely from experiments. Based on the flexibility and programmability of the bilayer, more complex shape-morphing architectures are predictably constructed by designing different geometries and distributions of the patterns, as we show through specific illustrative examples. This unique strategy, which integrates easy-to-process

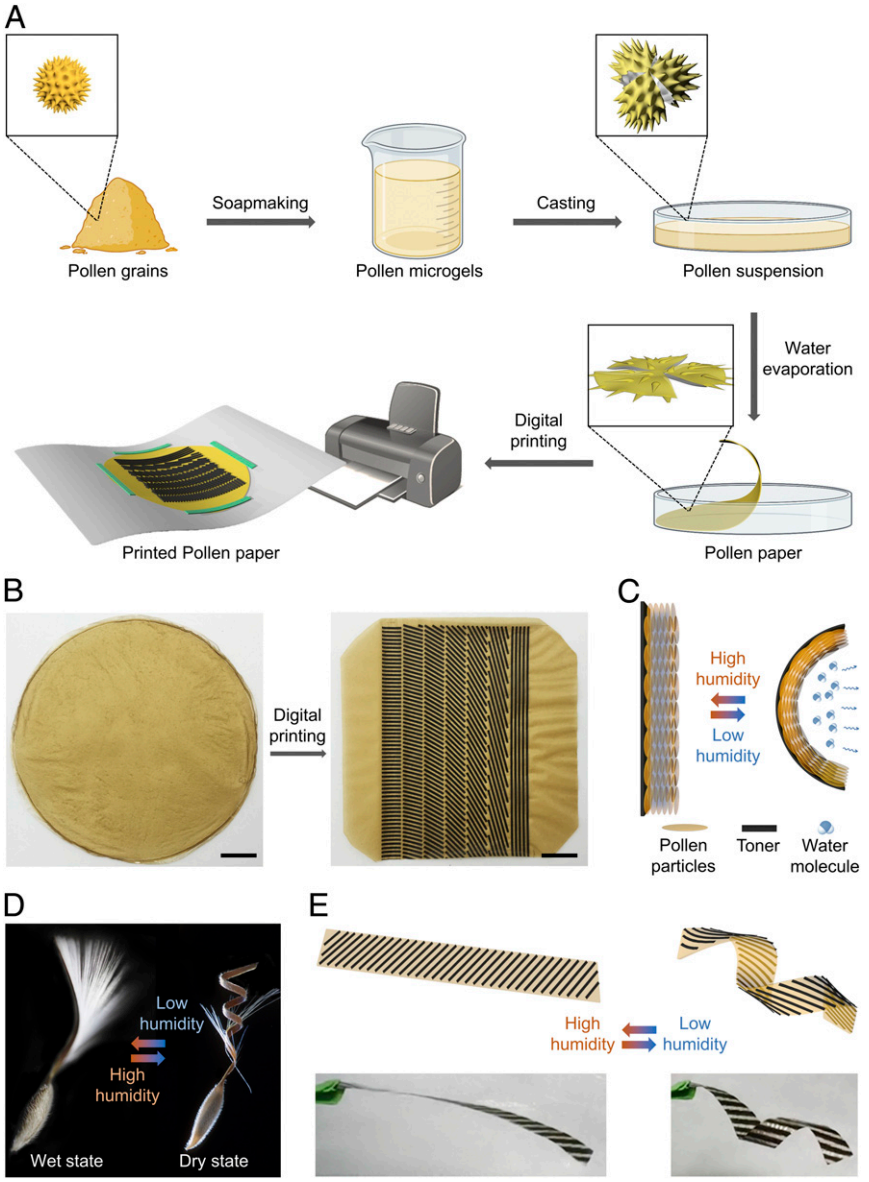

Fig. 1. Biomimetic autonomous shape-morphing deformation of humidity-responsive pollen paper. (*A*) Schematic illustration of toner-patterned pollen paper fabrication through pollen microgels suspension casting and direct digital printing. (*B*) A customized pollen bilayer was fabricated by direct digital printing with patterns using toner. (Scale bar, 1 cm.) (*C*) Schematic illustration of the strain mismatch created by water adsorption and desorption in the bilayer comprising the hydrophilic pollen paper and the hydrophobic ink pattern of styrene acrylate copolymer (introduced through the laser toner). (*D*) The awn of an individual seed exhibiting straight and coiling morphology, depending on changes in humidity. Image credit: Shutterstock / Emily Eriksson and Coulanges. (*E*) A ribbon-shaped pollen paper (3 cm × 0.5 cm) printed with a specific toner stripe pattern self-coiled in response to humidity stimulation. *Top* represents schematic illustration, and *Bottom* shows corresponding photographs from experiments.

pollen biomaterials of unique hygroresponsiveness with cost-effective digital printing, holds the promise of fabricating highly controllable shape-morphing materials using scalable and sustainable approaches.

Results and Discussion

The bilayer film was fabricated by simple digital printing of the pollen-based natural materials, as shown in Fig. 1*A*. We first made a flexible two-dimensional (2D) pollen paper using two steps: traditional soapmaking and subsequent pollen suspension casting, as described previously (38). Then, through general digital printing, a passive layer of patterns of digitally printable ink was printed onto the pollen paper. Owing to its ease of access and customizability, laser or inkjet printing technology facilitates the direct transfer of various digitally custom-designed patterns onto pollen papers (Fig. 1*B*). Considering the hygroexpansibility of the pollen paper (38) and the hygroinertness of the digitally printed patterned layer, it is hypothesized that the bilayer would curl upon exposure to low RH due to the strain mismatch induced by the asymmetrical hygroresponsiveness of the two layers (Fig. 1*C*). Compared with the plain pollen paper, the printed pollen paper exhibited a noticeable increase in water contact angle, indicating increased hydrophobicity, as anticipated (40) (*SI Appendix*, Fig. S1). When a pollen paper, with only half of the page printed with toner, was exposed to low RH, we observed that the printed part curled toward the pollen layer side, while the part without toner

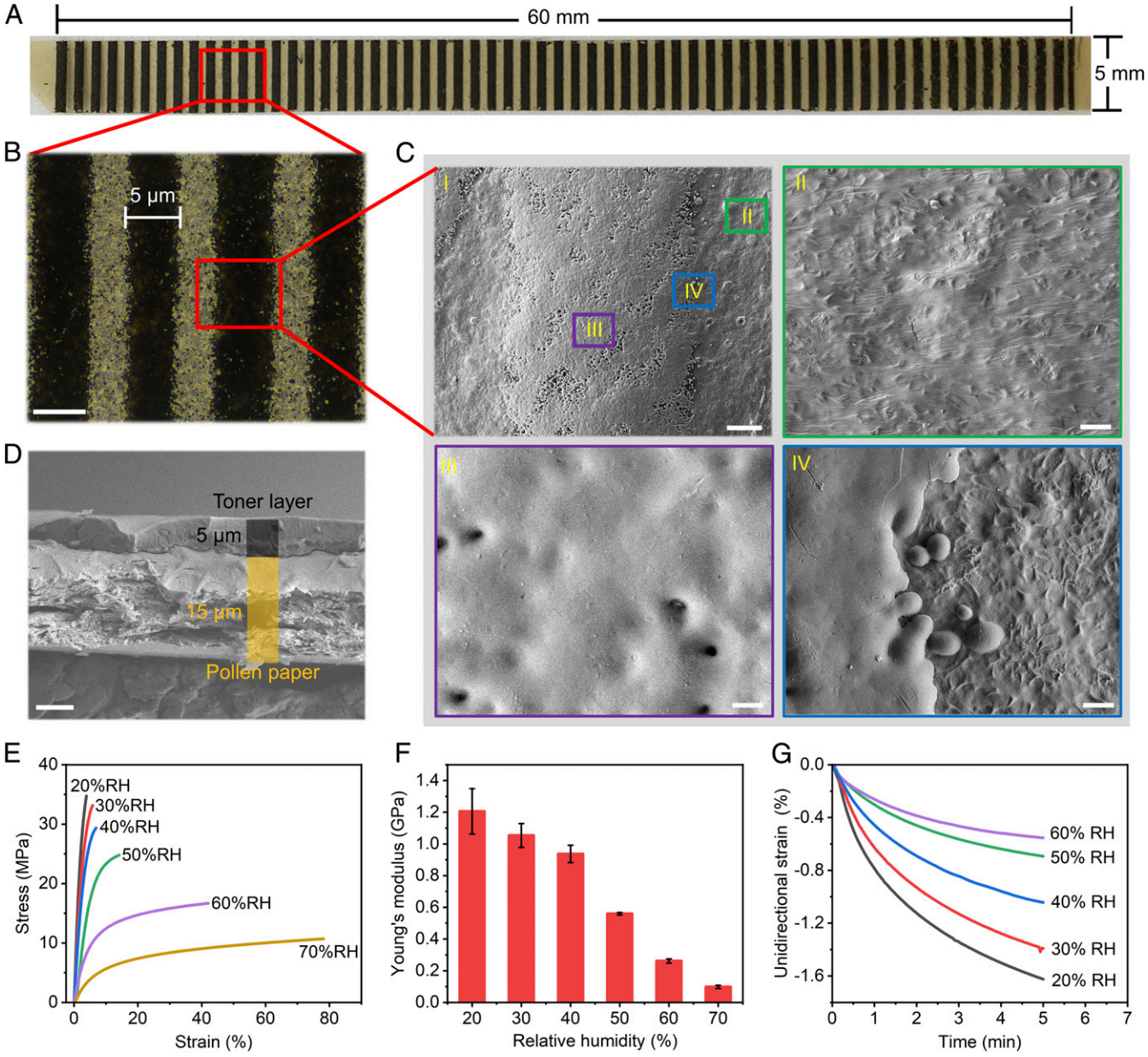

Fig. 2. Characterizations of the patterned pollen bilayer. (*A*) A photograph of a ribbon-shaped patterned pollen paper with a (*B*) close-up showing four parallel printed lines on the surface. (Scale bar, 0.5 mm.) (*C*) (*I*) Single stripe on pollen paper and magnification of three areas: (*II*) surface of pollen paper; (*III*) surface of printed toner, and (*IV*) the interface of pollen paper and toner. (Scale bars, 100 μm in *I* and 10 μm in *II*, *III*, and *IV*.) (*D*) Cross-section SEM image of the interface between the toner and pollen layer. (Scale bar, 5 μm.) (*E*) The representative stress–strain curves of the plain pollen paper were measured in uniaxial tensile tests under different controlled RH levels. (*F*) Young's modulus of pollen paper calculated from stress–strain curves under different RH levels. Samples were prepared in triplicate; error bars represent ±1 SD. (*G*) Shrinkage of the plain pollen paper upon reducing RH from 70% to lower levels led to autonomous contraction as a function of time, as shown from uniaxial strain measurements under zero applied stress.

remained unbent because of the differences in volume change between the two layers due to different levels of water absorption (*SI Appendix*, Fig. S2).

In the plant kingdom, hygromorphic responses are observed as strategies developed through evolution in various seed dispersal systems (41–43) that exhibit different mechanical deformation modes (44, 45). This is driven by the differential response of various tissue architectures to changes in ambient RH levels. Self-sowing is a characteristic of the *Pelargonium* plant species' awn that exhibits macroscopic reversible coiling deformation when exposed alternately to dry and wet environments (Fig. 1*D*) (46). This deformation strongly depends on the tilted orientation of the cellulose surrounding the cylindrical cells as a hygroactive layer in the awn (47). Here, inspired by the self-coiling of *Pelargonium* awn, we aligned the geometrical orientations of toner stripe patterns on the pollen paper to mimic the typical tilted architecture of the cellulose microfibrils in the awn and realized the replication of its reversible coiling deformation (Fig. 1*E*). The strategy adopted here thus illustrates a time-saving and highly customizable process for producing moisture-responsive bilayer materials capable of complex and programmable shape morphing.

As shown in Fig. 2*A*, we cut off a rectangular ribbon of the patterned bilayer for microstructural characterization, where the stripe pattern was printed with toner over predesigned width and spacing, both 500 μm (Fig. 2*B*). In the magnified view of a single toner line on pollen paper (Fig. 2 C, *I*), the two parallel edges of the toner line with a width of ∼500 μm are visible, which indicates the reliability of precision printing. In Fig. 2 C, *II*, a naturally wrinkled surface microtopography was observed (38). Additionally, cross-sectional microscopy demonstrates good conformal contact between the patterned and pollen layers (Fig. 2 *C*, *III* and *IV* and *D*). The pollen paper's surface microroughness promotes interlayer adhesion, which contributes to the mechanical integrity of the bilayer (*SI Appendix*, Fig. S3).

To elucidate shape evolution during the hygromorphic deformation of the bilayer, it is necessary to examine the changes in the mechanical and physical characteristics of the active layer, that is, the pollen paper, in response to changes in RH. Fig. 2*E* shows the stress–strain response of the plain pollen paper as a function of RH in a uniaxial tensile test. It is evident here that an increase in RH from 20% to 70% leads to a monotonic increase in the deformability and strain to failure of the pollen paper. This arises from the weakening induced by moisture absorption and a corresponding reduction in the yield and tensile strength values. Young's modulus values calculated from the initial linear slopes of the corresponding stress–strain curves showed a reduction as the RH increased (Fig. 2*F*). The loss of water molecules upon a change in RH from 70% to different lower levels caused the pollen paper to shrink. This unidimensional change was measured unidirectionally in the absence of an externally imposed load or stress. We calculated the corresponding strain based on a change in length over the original reference length at 70% RH, which is shown in Fig. 2*G* and *SI Appendix*, Fig. S4. By fitting the data with a polynomial function, we established the relationship between a specific RH value and the corresponding unidirectional strain in pollen paper (*SI Appendix*, Fig. S5). These results provide a quantitative basis to predict and custom-design three-dimensional (3D) shapes through autonomous responses to controlled humidity levels.

We now demonstrate how the bilayer ribbon's coiling morphology can be controlled by adjusting the orientation of the stripe patterns. Fig. 3*A* schematically illustrates key geometric parameters and the associated nomenclature for planar and coiled configurations of the tailored patterned bilayer ribbon, where radius (r) is the cylinder radius and pitch (p) is the distance between two successive turns of the curve of pollen ribbon, measured parallel to the coiling axis. Images of four bilayer ribbons with different toner pattern orientation angles (θ) from 0° to 90° are shown in Fig. 3*B*. The self-coiling shape evolution processes of the bilayers, which evolve autonomously in response to a reduction in RH from about 70% to about 20%, for three different orientation angles (30°, 60°, and 90°) of the toner stripe patterns are shown in Fig. 3*C*. Semiquantitative details of how the geometrical parameters evolve during the autonomous hygromorphing of the patterned bilayer were also obtained from the experiments. As shown in Fig. 3 *D* and *E*, both the coiling diameter and pitch decreased as a function of time, where the diameter of all samples almost reached similar steady states within 5 min. These results show that the orientation of toner stripe patterns can markedly influence shape evolution.

The observed shape evolution is primarily a consequence of the inactive layer's strong mechanical constraining effect on the deformation of the active pollen paper. The geometric orientation of the pattern represented by the angle θ strongly influences the directionality and degree of constraint. This trend is analogous to the process of shape evolution in thin films, where the orientation of patterned lines on substrates (commonly encountered in microelectronic devices) can influence the evolution of substrate curvature and shape due to thermal mismatch between the layers (48, 49). When the patterned line was printed parallel to the short side of the pollen paper strip (i.e., $\theta = 0°$), the sample coiled along the short axis (Movie S1). When the line was printed perpendicular to the short side of the paper (i.e., $\theta = 90°$), the sample coiled along the long axis, leading to a ring morphology (Movie S2). For $0° < \theta < 90°$, the sample assumed a coiled helical morphology, where shorter helices formed at higher values of θ (Fig. 3*C* and Movie S2). As the RH was increased from 20% to 70% upon reintroduction of moisture, complete reversibility of deformation and shape was observed as shown in *SI Appendix*, Fig. S6 and Movie S3. Note that the time to uncoil and reverse deformation upon an increase in RH is longer than during coiling, because of the asymmetry in moisture absorption and desorption kinetics (*SI Appendix*, Fig. S7) (50). The effects of other orientation angles (θ) of 15°, 45°, and 75° on moisture-dependent shape evolution are illustrated in *SI Appendix*, Fig. S8.

To further elucidate the hygromorphing process, we modeled mismatch-induced self-coiling behavior as shape transformation driven by differential thermal expansion by employing FEM (51–53). Details of the simulation and the underlying assumptions are provided in *Materials and Methods*. From both experimental and simulation results, the variations in coiling diameter and pitch as functions of θ are plotted at a fixed RH of about 20% in Fig. 4*A*. The pitch values decreased with increasing θ, while the diameter remained relatively unaltered. During dehydration, the pollen paper's shrinkage drives the structure to bend toward the pollen paper side, and the axis of the coil is always perpendicular to the planes defined by each toner line. As demonstrated in Fig. 4*B*, when $\theta = 0°$, the long side of the bilayer ribbon curled up; when $0° < \theta < 90°$, the ribbon deformed into a coiled helical structure; when $\theta = 90°$, the short side curled up. The match between simulation results and experimental observation allows us to predict the coiling deformation with high fidelity. A higher toner coverage ratio can increase the strain mismatch between the toner and pollen layers during dehydration, leading to the bilayer's tighter coiling. For a particular choice of geometrical parameters (length: 10 mm; width: 5 mm) with $\theta = 90°$ at RH of ∼20%, the bending curvature ($1/r$) increased from about 4 cm^{-1} to 8 cm^{-1} with an increase in the toner coverage ratio from 20% to 80% (*SI Appendix*, Fig. S9). Compared with other hygroresponsive shape-morphing materials, our toner/pollen bilayers exhibit enhanced actuation ability, as summarized in *SI Appendix*, Table S1.

The RH level is another critical factor influencing deformation, because the pollen layer has an RH-dependent strain (*SI Appendix*, Fig. S5). Fig. 4*C* reveals the rise in both pitch and

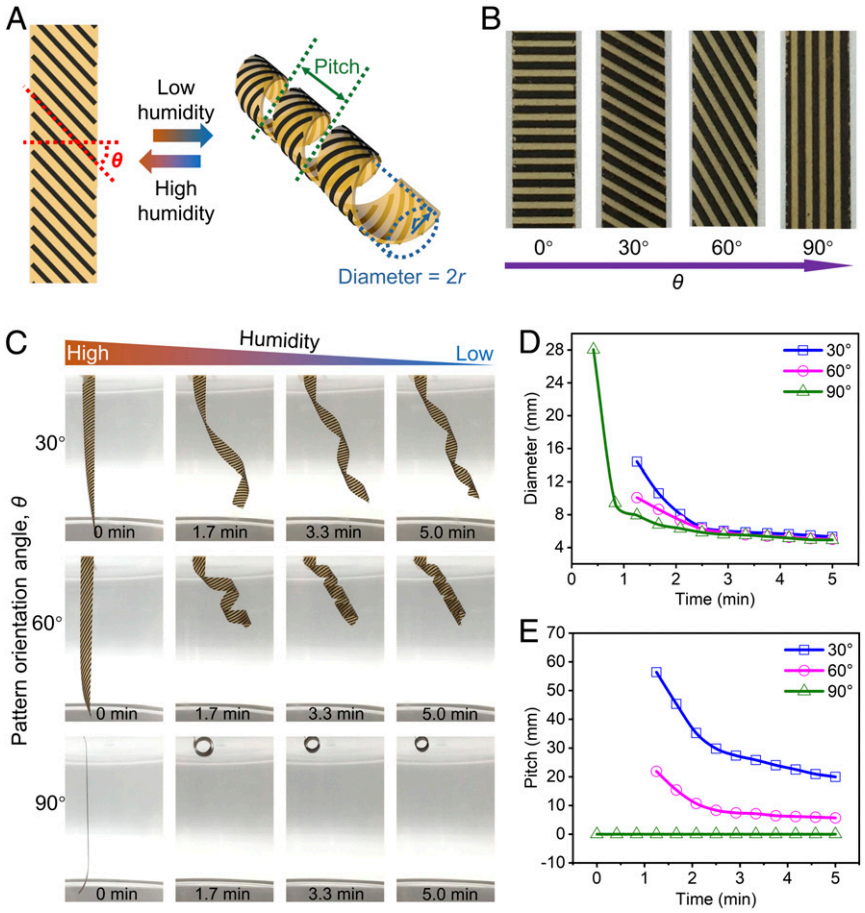

Fig. 3. Bioinspired self-coiling morphology induced by the change in RH. (*A*) Schematic illustration of bioinspired coiling geometry and nomenclature of the patterned bilayer ribbon. (*B*) Images of bilayer ribbons with different toner pattern orientation angles, θ. (*C*) Programed self-coiling processes of the patterned bilayer ribbons with three different values of θ in response to RH changes from ~70% to ~20%. (*D* and *E*) Evolution of coiling diameter (*D*) and pitch (*E*) as a function of time for three different values of the pattern orientation angle (θ).

diameter values with RH level for $\theta = 45°$ (Movie S4). FEM predictions reveal that the helical structure's diameter is inversely proportional to the bilayer's strain mismatch level, irrespective of the toner pattern orientation (*SI Appendix*, Fig. S10*A*). In contrast, the pitch is determined collectively by the pattern orientation and strain mismatch level, which could be obtained through the relationship $p = 2\pi r \tan(90° - \theta)$ (*SI Appendix*, Fig. S10*B*). The contour plot in Fig. 4*D* illustrates how the pitch varies with θ and RH. For fixed θ, the pitch was reduced with a decrease in the RH level. The diameter also followed a similar trend; for a fixed RH level, the pitch decreased with an increase in θ, while the diameter remained nearly the same, as shown in *SI Appendix*, Fig. S11. Our experiments and simulations reveal a direct causal relationship between the coiling level and the residual stress caused by the strain mismatch between the pollen paper and the pattern layer for different values of RH.

With digital printing, the pattern can be designed onto the pollen paper to customize complex hygromorphic configurations. We demonstrate this capability through experiments designed to produce complex shapes found in nature. As shown in Fig. 5*A*, 3D configurations of the patterned pollen paper bilayers with multiple coiling modes were achieved by integrating two stripe patterns of distinctly different orientations (Fig. 5 *A*, *Left*) or even opposite orientations (Fig. 5 *A*, *Middle*). Furthermore, sequentially arranging the patterns of orientations from 15° to 90° into one ribbon generated a coiling structure with gradient pitches in response to the low RH (Fig. 5 *A*, *Right*). By distributing and tailoring these pattern units, we successfully reproduced the complex morphology of the flower orchid *Dendrobium helix*, which consists of six petals and four different types of configuration units, as shown in Fig. 5 *B*, *I*. When the initially planar sample (Fig. 5 *B*, *II*) was exposed to low RH, the discretely patterned bilayer in each "petal" morphed into desired 3D shapes. It, together, formed a complete "flower." Fig. 5 *B*, *III* and *IV* showed the top and side views of the complex biomimetic shape, respectively, which resembled a blooming orchid (Movie S5).

As a result of its remarkable shape-morphing ability, the patterned bilayer with the pollen paper as a substrate has the potential to act as an active and dynamic hinge to rotate two connected pieces of pollen paper through a programmable bending angle made possible by locally printed pattern geometries, as shown in Fig. 6*A*. It is found that the bending angle α depends on the length of the pattern, in which a length of even only 2 mm can achieve a bending angle of about 90°. By combining this strategy with the paper's geometric design, we are able to create a 3D square box (2 mm) or a triangular pyramid (2.5 mm), whose closing and opening are triggered by a change in RH (Fig. 6*B* and *SI Appendix*, Figs. S12 and S13 and Movie S6). The flexibility of this design and printing strategy to produce "box-like" structures also illustrates pathways to convenient digital manufacturing of containers (such as boxes, cups, bowls, etc.) made of natural materials that are economical, environmentally friendly, and amenable to large-volume production.

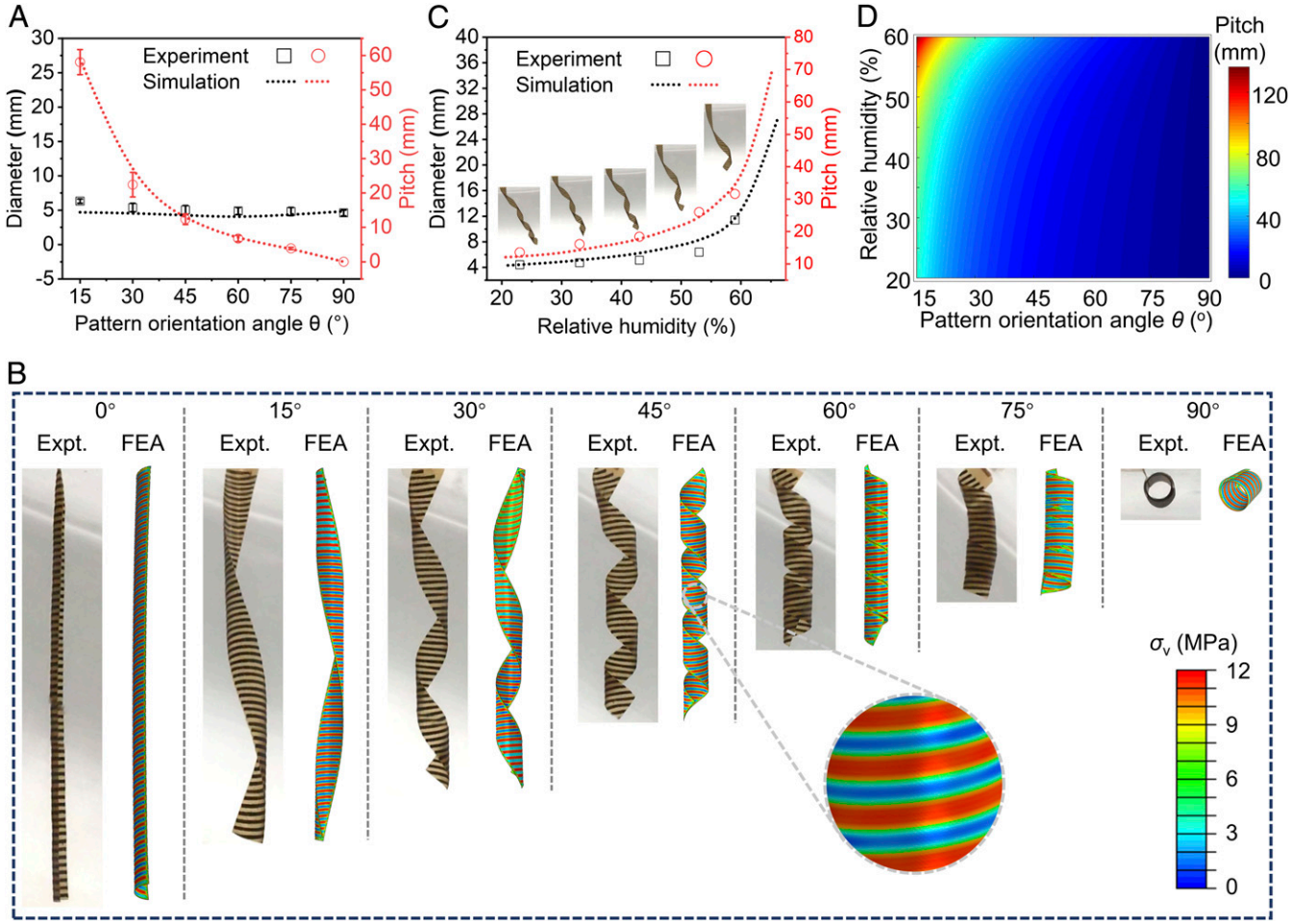

Fig. 4. Quantitative analysis of fundamental geometrical parameters with FEA. (*A*) Variation of diameter and pitch of the coiling shape as a function of pattern orientation angle θ in response to the RH of ~20%. Samples were prepared in triplicate. The dashed lines show the results obtained from the FEA simulations, and the symbols represent experimental observations (Expt.). (*B*) Patterned bilayer ribbons coiling to varying degrees achieved by designed θ at RH of ~20%. For each θ, experimental observation (*Left*) and the corresponding simulation result (*Right*) are shown together. A higher magnification view of the simulation for the 45° orientation angle is also shown to highlight the iso-contours of von Mises stress (σ_v). (*C*) Variation of diameter and pitch of the coiling shape as a function of RH level at pattern orientation angle θ of 45°. The dashed lines show the results obtained from the FEA simulations, and the symbols represent experimental observations. (*D*) Contour plot of the pitch varying as functions of pattern orientation angle θ and RH levels.

Our results also show that the pollen papers on both sides of the hinge fold autonomously at a certain angle (denoted as folding angle β) when the orientation angle of the pattern is less than 90°, as shown in Fig. 6*C*. Therefore, it is feasible to realize complex programmable hygromorphic configurations by customizing the distribution and orientation of discrete patterns. For example, a single pollen paper ribbon with two identical patterns with folding angles of 60° would deform into a shape of "N" (Fig. 6 *D*, *Left* and Movie S7). Based on the same scheme, the letters "T" and "U" were also generated (Fig. 6 *D*, *Middle* and *Right*).

The discussion thus far has demonstrated the feasibility of producing complex shapes on demand and autonomously. This is achieved through humidity-responsive shape evolution in a natural substrate, on which shape-specific patterns can be strategically designed and deposited by recourse to routine digital printing. Once this plant-based material is made, it is necessary to ensure that any further change in shape does not occur during the service use of this "product," the conditions for which, inevitably, will require moderate to severe changes in humidity (as in, for example, the case of a food container used for a hot or cold liquid, or a box or envelope being transported in humid weather). It is, therefore, important to address the following question: Once a complex shape is designed and fabricated with the shape-morphing natural material, can the digitally printed hygromorphic shape be "frozen" so that no further effect of humidity occurs in influencing the geometry and shape? We now show that this is indeed possible, with an illustrative example.

The patterned pollen substrate bilayer subjected to a humid environment should be protected with a further coating, to impart the fabricated shape sufficient hygrophobicity and immunity to further changes in shape or geometry arising from variation in humidity. Here we demonstrate the feasibility of achieving this by selecting chitosan, a ubiquitous polycationic biopolymer. Since substantial anionic surface charge exists with the KOH-incubated pollen particles, chitosan was chosen to form an electrostatic biocomposite with the pollen paper and blocks its hydrophilic carboxylic acid functional groups.

Fig. 7*A* shows that the original (untreated) pollen paper, after being incubated in chitosan solution overnight and then washed three times in deionized (DI) water and dried under ambient conditions, exhibits only a small change in size or shape. The low molecular weight chitosan solution (2 wt%) was prepared by dissolving 2 g of chitosan in 98 mL of acetic acid aqueous solution (1% vol/vol). Hygroexpansion after this treatment was quantified experimentally in terms of uniaxial strain arising from shrinkage

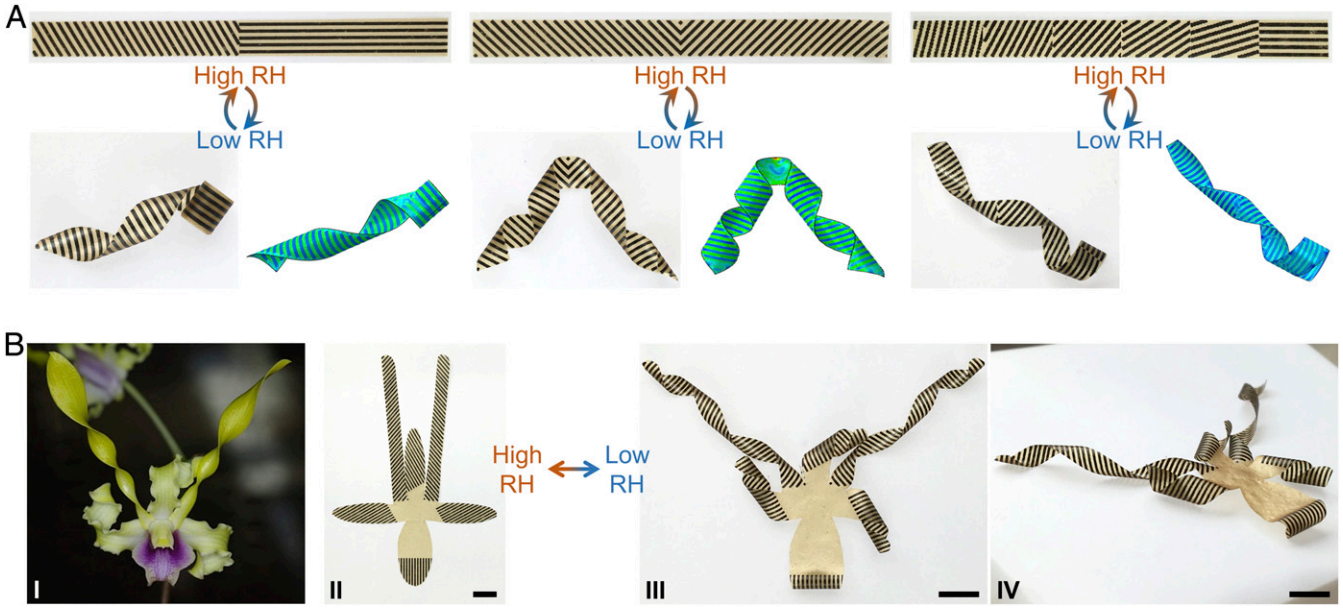

Fig. 5. Complex hygromorphic deformation enabled through digital design of patterned bilayer units. (*A*) The 3D configurations of the bilayer ribbons with multiple coiling modes. For each of the three shapes of interest (*Left*, *Middle*, and *Right*), the experimental and simulation (in teal color) results are shown on the *Bottom Left* and *Bottom Right*, respectively. (*B*) A bilayer-based biomimetic orchid *Dendrobium helix* in response to low RH level. (*I*) An image of the *Dendrobium helix* found in nature (image from ref. 56). Image credit: Paul Zorn (photographer); (*II*) initial hydrated flat state; and (*III* and *IV*) top view and side view of the dehydrated "blooming" state, respectively. (Scale bars, 1 cm.)

for the original (untreated) and chitosan-treated pollen paper as a function of time upon reducing the RH from 70% to 20%. As envisioned, the treated pollen paper underwent uniaxial contraction of only about 0.3% with change in RH from 70% to 20%, less than one-fifth of that seen in the untreated, original pollen paper (Fig. 7*B*). Also note that this behavior of the chitosan-treated pollen paper is essentially the same as that of commercially available general office A4-size paper (made of wood products). The chitosan-treated pollen paper still maintains good flexibility and printability. Next, we tested the hygroresponsive behavior of the chitosan-treated pollen paper, printed with specific toner patterns, as shown in Fig. 7*C* and Movie S8. The digital printing process of the chitosan-treated pollen paper was the same as that for the untreated original paper. The chitosan-treated sample remained relatively stable in shape during large variations in RH, while the original, untreated pollen paper curled autonomously, as expected. Further, we demonstrated that coating the pollen paper with a thin layer of petroleum jelly can "freeze" the complex shape

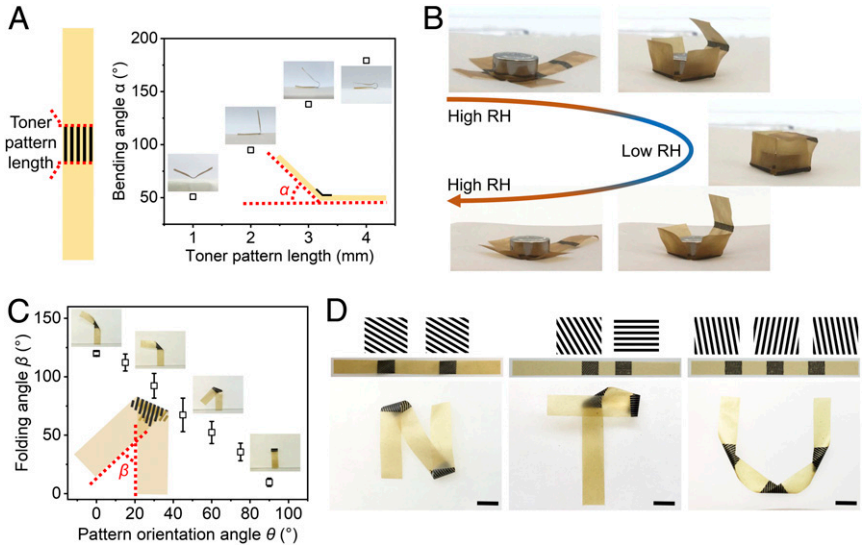

Fig. 6. Patterned bilayer as a dynamic hinge for programmable folding. (*A*) Variation of bending angle α as a function of toner pattern length in response to the RH of ~20%. (*B*) Reversible closing and opening of a 3D square box triggered by the change in RH level where the short-patterned bilayers are hinges that dynamically respond to moisture level change. (*C*) Variation of folding angle β as a function of toner pattern orientation angle θ responds to the RH of ~20%. Samples were prepared in triplicate. (*D*) (*Bottom*) Self-morphing of pollen paper ribbons into the shape of the letters (*Left*) "N," (*Middle*) "T," and (*Right*) "U" of the alphabet through the customized distribution of discrete toner patterns. (*Top*) The schematic stripe patterns indicate the orientations of the discrete toner patterns. (Scale bar, 5 mm.)

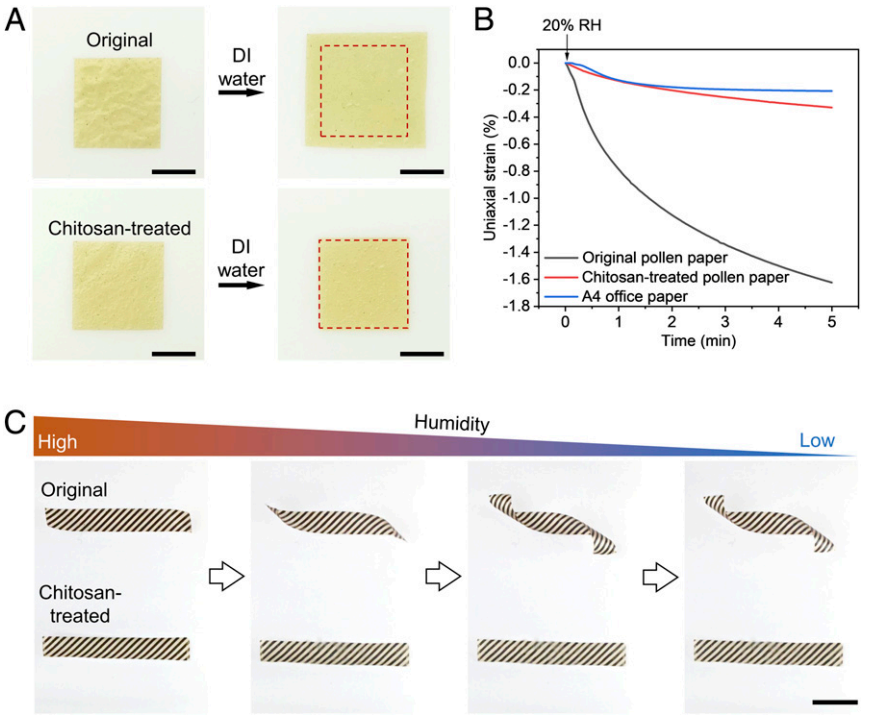

Fig. 7. Turning off the deformability of the toner/pollen paper bilayer. (*A*) Photographs showing the different swelling between the original and chitosan-treated pollen paper after water immersion. (Scale bar, 1 cm.) (*B*) Shrinkage of the plain original and chitosan-treated pollen paper upon reducing RH from 70% to 20% as a function of time, as shown from uniaxial strain measurements. (*C*) Original (untreated) and chitosan-treated pollen ribbons printed with toner patterns exhibited coiling and noncoiling, respectively, in response to RH change. (Scale bar, 1 cm.)

of the paper and render the paper insensitive to changes in humidity, as shown in *SI Appendix*, Fig. S14 (Movie S9). Therefore, through conventional coating techniques, we can effectively turn off the autonomous shape change when it is not desired.

The demonstration of the digital printing of shape-morphing natural materials in the foregoing discussion entailed use of standard laser toner as the patterning material for the inactive layer on the pollen substrate. This was to illustrate how simple and widely available digital tools can be deployed to achieve the approaches proposed here. We have shown that natural biomaterials can be used as printable ink using standard inkjet, laser, or 3D printers, to create the inactive layer patterns on the pollen substrate, instead of a material such as laser toner. *SI Appendix*, Fig. S15 shows a variety of patterns digitally printed (using a standard inkjet printer, HP Envy Photo 6220, HP Inc.) onto the pollen paper where the material used for patterning was edible ink (66.9% water, 18% propylene glycol, 10% glycerin, 3.5% amaranth, and 1.6% erioglaucine, by wt%) for the inactive layer. Measurement of the wetting angle (62.5° ± 2.2°) from water droplet contact on the pollen paper printed with edible ink supported the hygrophobicity of the patterned layer. To this end, we used the pollen paper to fabricate a paper cup and straw based on an origami method, as shown in *SI Appendix*, Figs. S16 and S17.

Conclusion

We have demonstrated that natural, nonallergenic pollen can be combined with conventional digital printing technology to fabricate moisture-responsive bilayer materials with complex deformability and functional programmability. Various patterns with predesigned geometries and distributions could be directly printed onto pollen papers to achieve shape-morphing 3D configurations through a commercial digital printer. Moreover, we have illustrated the feasibility of "freezing" the highly controllable shape changes to facilitate practical applications for different humidity levels. Importantly, the conversion of pollen microgel particles to paper is straightforward and technically simple and can be achieved using industrial processing machinery in an eco-friendly manner. Such possibilities are also compatible with further exploration of various paper parameters such as thickness and mechanical strength to modulate flexibility and responsiveness. As such, the strategy proposed here may hold promise for the sustainable development of intelligent green products with not only programmable and reversible mechanical properties but also functional characteristics useful in electronic and biomedical applications.

Materials and Methods

Materials. Sunflower bee pollens (*Helianthus annuus* L.) were purchased from Shaanxi GTL Biotech Co., Ltd. Acetone, diethyl ether, potassium hydroxide (KOH), chitosan (low molecular weight), and acetic acid were purchased from Sigma-Aldrich Pte Ltd. Nylon mesh was purchased from ELKO Filtering Co. LLC. Petroleum jelly is an odorless semisolid which consists of a mixture of hydrocarbons, which has a CAS number 8009-03-8.

Defatting Sunflower Bee Pollen. Sunflower bee pollen (250 g) was dispersed in DI water (1 L, 50 °C) and stirred. The mixture was passed through a 200-μm nylon mesh to remove sand and other contaminants. After suction filtration, the collected powder was mixed with acetone (500 mL) and refluxed for 3 h at 50 °C. This acetone washing step was repeated two times, until the color of the pollen powder was stable, and was then left in the fume hood overnight to evaporate the acetone fully. After that, the resultant pollen powder (20 g) was mixed with diethyl ether (250 mL) under stirring at room temperature for 2 h, repeated two times. Finally, the pollen powder was transferred to a Petri dish and left to completely dry in the fume hood to get the defatted pollen.

Pollen Microgels Preparation. Detailed steps for pollen microgels' preparation can be found in our recent work (38). Briefly, the defatted pollen (10 g) was mixed with KOH solution (10 wt% aqueous, 100 mL) under stirring for 2 h at 80 °C, followed by centrifuging at 4,500 rpm for 5 min. The precipitated sample was topped up and vortexed with a fresh 10% KOH solution, then centrifuged again. The KOH washing step was repeated five times to remove

the internal cytoplasm entirely. The washed sample was then resuspended with a fresh 10% KOH solution and left in a hot plate oven set to 80 °C for 12 h to implement the KOH incubation. After that, the resulting pollen suspension was neutralized with DI water to a PH of 7, centrifuged to collect the pollen microgels, and stored at 4 °C for further utilization.

Pollen Paper Fabrication. Preprepared pollen microgel was adequately resuspended in DI water and then was cast into a Petri dish to dry into a paper-like geometry in a dry box. After complete water evaporation, the paper was detached from the substrate's surface and kept at the ambient environment (the RH is around 70%).

Printing Commercial Hydrophobic Toner on Planar Pollen Paper. The desired patterns were prepared using AutoCAD 2018. The toner (HP 76× High Yield Black Original LaserJet Toner) patterns were printed on the pollen paper using a commercial laser printer (HP LaserJet Pro MFP M428fdn) at a resolution of 1,200 dpi. The toner composition is shown in *SI Appendix*, Table S2, according to the material safety data sheet (54). After printing, we tailored the toner-patterned pollen papers into expected shapes to be tested based on the predesigned layouts.

Water Contact Angle Measurement. The water contact angles of different samples' surfaces were determined by a tensiometer (Attension Theta, Biolin Scientific). One Attension software was employed to analyze the water drop shapes.

Characterization of Microstructure. Scanning electron microscopy (SEM) was used to observe the microstructure of the patterned bilayer film. Firstly, the samples tested were sputter-coated with gold (JEOL; operating settings) for 35 s. We then used a JSM-7600F Schottky field-emission scanning electron microscope (JEOL) to take the SEM images at an accelerating 5.00-kV voltage.

Thickness Measurements. The thicknesses of the bare pollen paper and the toner-covered pollen paper were measured by a micrometer (order no. 293-240-30, Mitutoyo Asia Pacific Pte Ltd.).

Tensile Testing. We used a dynamic mechanical analyzer (DMA Q800, TA Instruments) with RH control module (DMA-RH Accessory) to perform the tensile mechanical testing where all tests were carried at 28 °C. The gripped pollen paper sample (25 mm × 5 mm × 0.03 mm) was subjected to force at a rate of 1 N/min until failure under specific RH (20%, 30%, 40%, 50%, 60%, and 70%). Each test was repeated three times. The Young's modulus of the pollen paper was calculated from the slope of the elastic ranges in the stress–strain curves. All data were processed with universal analysis 2000 software (TA Instruments).

Measurement of the Hygroscopicity-Induced Unidirectional Strain of Pollen Paper Ribbons. A thin ribbon of pollen paper (25 mm × 5 mm × 0.03 mm) was mounted in a film tension clamp on the DMA Q800 equipped with the DMA-RH Accessory to control RH mentioned above. We measured pollen ribbons' contraction as the RH decreased from 70% to set values (20%, 30%, 40%, 50%, or 60%). Then, the following method program was employed: 1) stress = 0 MPa (removes all residual force); 2) equilibrate at 28.00 °C for 10 min, 3) measure length, 4) data storage, 5) RH x % (sets RH control, x = 20%, 30%, 40%, 50%, or 60%), and 6) isothermal for 10 min (allows time for the sample to equilibrate under set RH level).

The contraction was obtained from the strain recorded in the datasheet. The test was performed three times to get the average value.

Measurement of Young's Modulus of Toner. To measure Young's modulus of the toner, we obtained the value 4,096 of the force versus displacement (FD) curve using the atomic force microscopy (AFM, NX-10, Park Systems) in the area of 3 μm × 3 μm. The spring constant and deflection sensitivity of the AFM cantilever (AC160TS, a spring constant of ∼35 N/m) was calibrated by recourse to the thermal vibration using commercial software (SmartScan, Park Systems). The AFM cantilever was rinsed with water and ethanol and treated in an ultraviolet light cleaner for ∼30 min to eliminate any contamination on the tip. The Hertzian model is analyzed in the context of FD curves using a commercial software analysis program (SmartScan, Park Systems) for data analysis.

Coiling Behavior Testing of the Patterned Bilayer Ribbons Responding to Change in RH. Patterned bilayer ribbons (6 cm × 0.5 cm) were hung in a chamber. The specific RH levels were made by saturated salt aqueous solutions, for example, CH_3COOK (RH = 23%), $MgCl_2$ (RH = 33%), K_2CO_3 (RH = 43%), $Mg(NO_3)_2$ (RH = 53%), NaBr (RH = 59%), and KI (RH = 70%). These whole processes were recorded by an iPhone 6s (1,920 × 1,080-pixel resolution, 60 frames per second, Apple Inc.).

Computational Analysis. Finite element analysis (FEA) was conducted by using the commercially available package Abaqus (55). We modeled the coiling behavior as a differential thermal expansion-driven shape transformation problem (51–53). More specifically, a hypothetical negative thermal expansion coefficient was assigned to the pollen paper to mimic its shrinkage during dehumidification. The system temperature gradually increased from zero to a final value that would lead to a thermal strain equivalent to the strain caused by dehydration as measured in experiments. The thermal strain produced in toner was kept at zero by assigning a zero thermal expansion coefficient in all the simulations. The strain mismatch between the pollen paper and toner layers is responsible for the ribbons' 3D coiling. It was modeled as a bilayer structure with toner and pollen paper as the top and bottom layers. Based on experimental measurements, the thickness of the pollen paper and toner was set as 30 and 5 μm, respectively, in our simulations. Following the experimental setup, the samples with different orientations of toner patterns were simulated. The pattern orientation angles between the toner strips and the short side of the pollen paper varied from 0° to 90°. A combination of homogeneous (for regions without toner) and composite (for regions with toner) shell sections was used in the simulations. The dimensions and properties of the pollen paper and toner were summarized in *SI Appendix*, Table S3. The toner/pollen structure was meshed using an eight-node doubly curved thin shell with reduced integration shell elements (S8R5). A fixed boundary condition was applied at the middle point of one end to avoid any possible rigid body motion.

Chitosan Treatment. At first, 2% wt/vol chitosan solution was prepared by dissolving 2 g of chitosan, low molecular weight, in acetic acid aqueous solution (1% vol/vol). Then, the resultant original pollen papers were submerged into the chitosan solution overnight, followed by washing three times with DI water. After drying, the chitosan-treated pollen papers were obtained.

Data Availability. All study data are included in the article, *SI Appendix*, and Movies S1–S9.

ACKNOWLEDGMENTS. This work was supported by the National Research Foundation Competitive Research Programme Grant NRF-CRP10-2012-07. Z.Z. and S.S. were supported by Nanyang Technological University, Singapore, with S.S. holding a Distinguished University Professorship.

1. N. A. Carter, T. Z. Grove, Protein self-assemblies that can generate, hold, and discharge electric potential in response to changes in relative humidity. *J. Am. Chem. Soc.* **140**, 7144–7151 (2018).
2. L. Zhang, P. Naumov, Light- and humidity-induced motion of an acidochromic film. *Angew. Chem. Int. Ed. Engl.* **54**, 8642–8647 (2015).
3. J. Troyano, A. Carné-Sánchez, D. Maspoch, Programmable self-assembling 3D architectures generated by patterning of swellable MOF-based composite films. *Adv. Mater.* **31**, e1808235 (2019).
4. Y. Dong *et al.*, Multi-stimuli-responsive programmable biomimetic actuator. *Nat. Commun.* **10**, 4087 (2019).
5. H. Deng *et al.*, An instant responsive polymer driven by anisotropy of crystal phases. *Mater. Horiz.* **5**, 99–107 (2018).
6. H. Cheng *et al.*, One single graphene oxide film for responsive actuation. *ACS Nano* **10**, 9529–9535 (2016).
7. E. Steven *et al.*, Silk/molecular conductor bilayer thin-films: Properties and sensing functions. *Mater. Horiz.* **1**, 522–528 (2014).
8. X. P. Hao *et al.*, Kirigami-design-enabled hydrogel multimorphs with application as a multistate switch. *Adv. Mater.* **32**, e2000781 (2020).
9. Y. Liu *et al.*, Humidity- and photo-induced mechanical actuation of cross-linked liquid crystal polymers. *Adv. Mater.* **29**, 1604792 (2017).
10. L. Wang, D. Chen, K. Jiang, G. Shen, New insights and perspectives into biological materials for flexible electronics. *Chem. Soc. Rev.* **46**, 6764–6815 (2017).
11. J.-N. Ma *et al.*, Programmable deformation of patterned bimorph actuator swarm. *Natl. Sci. Rev.* **7**, 775–785 (2020).
12. L. Zhang, X. Qiu, Y. Yuan, T. Zhang, Humidity- and sunlight-driven motion of a chemically bonded polymer bilayer with programmable surface patterns. *ACS Appl. Mater. Interfaces* **9**, 41599–41606 (2017).
13. J. B. Zimmerman, P. T. Anastas, H. C. Erythropel, W. Leitner, Designing for a green chemistry future. *Science* **367**, 397–400 (2020).
14. R. Vermeulen, E. L. Schymanski, A. L. Barabási, G. W. Miller, The exposome and health: Where chemistry meets biology. *Science* **367**, 392–396 (2020).

15. P. J. Landrigan *et al*., The Lancet Commission on pollution and health. *Lancet* **391**, 462–512 (2018).
16. M. Faria, M. Björnmalm, E. J. Crampin, F. Caruso, A few clarifications on MIRIBEL. *Nat. Nanotechnol.* **15**, 2–3 (2020).
17. Y. Lin *et al*., Blood exposure to graphene oxide may cause anaphylactic death in non-human primates. *Nano Today* **35**, 100922 (2020).
18. Q. Zhu, Y. Jin, W. Wang, G. Sun, D. Wang, Bioinspired smart moisture actuators based on nanoscale cellulose materials and porous, hydrophilic EVOH nanofibrous membranes. *ACS Appl. Mater. Interfaces* **11**, 1440–1448 (2019).
19. P. Bettotti *et al*., Dynamics of hydration of nanocellulose films. *Adv. Mater. Interfaces* **3**, 1500415 (2016).
20. Q. Zhu *et al*., Stimuli-responsive cellulose nanomaterials for smart applications. *Carbohydr. Polym.* **235**, 115933 (2020).
21. T. Wu *et al*., A bio-inspired cellulose nanocrystal-based nanocomposite photonic film with hyper-reflection and humidity-responsive actuator properties. *J. Mater. Chem. C Mater. Opt. Electron. Devices* **4**, 9687–9696 (2016).
22. K. Zhang *et al*., Moisture-responsive films of cellulose stearoyl esters showing reversible shape transitions. *Sci. Rep.* **5**, 11011 (2015).
23. L. Zhang, H. Liang, J. Jacob, P. Naumov, Photogated humidity-driven motility. *Nat. Commun.* **6**, 7429 (2015).
24. T. Jia *et al*., Moisture sensitive smart yarns and textiles from self-balanced silk fiber muscles. *Adv. Funct. Mater.* **29**, 1808241 (2019).
25. S. Lin, Z. Wang, X. Chen, J. Ren, S. Ling, Ultrastrong and highly sensitive fiber microactuators constructed by force-reeled silks. *Adv. Sci. (Weinh.)* **7**, 1902743 (2020).
26. D. Liu *et al*., Spider dragline silk as torsional actuator driven by humidity. *Sci. Adv.* **5**, eaau9183 (2019).
27. X. Chen *et al*., Scaling up nanoscale water-driven energy conversion into evaporation-driven engines and generators. *Nat. Commun.* **6**, 7346 (2015).
28. X. Chen, L. Mahadevan, A. Driks, O. Sahin, Bacillus spores as building blocks for stimuli-responsive materials and nanogenerators. *Nat. Nanotechnol.* **9**, 137–141 (2014).
29. W. Wang *et al*., Harnessing the hygroscopic and biofluorescent behaviors of genetically tractable microbial cells to design biohybrid wearables. *Sci. Adv.* **3**, e1601984 (2017).
30. M. Wang, X. Tian, R. H. A. Ras, O. Ikkala, Sensitive humidity-driven reversible and bidirectional bending of nanocellulose thin films as bio-inspired actuation. *Adv. Mater. Interfaces* **2**, 1500080 (2015).
31. L. Zhang, S. Chizhik, Y. Wen, P. Naumov, Directed motility of hygroresponsive biomimetic actuators. *Adv. Funct. Mater.* **26**, 1040–1053 (2016).
32. O. Cakmak, H. O. El Tinay, X. Chen, O. Sahin, Spore-based water-resistant water-responsive actuators with high power density. *Adv. Mater. Technol.* **4**, 1800596 (2019).
33. Y. Kuang *et al*., Selectively aligned cellulose nanofibers towards high-performance soft actuators. *Extreme Mech. Lett.* **29**, 100463 (2019).
34. R. M. Erb, J. S. Sander, R. Grisch, A. R. Studart, Self-shaping composites with programmable bioinspired microstructures. *Nat. Commun.* **4**, 1712 (2013).
35. Z. J. Wang, C. N. Zhu, W. Hong, Z. L. Wu, Q. Zheng, Cooperative deformations of periodically patterned hydrogels. *Sci. Adv.* **3**, e1700348 (2017).
36. L. Zhang, P. Naumov, X. Du, Z. Hu, J. Wang, Vapomechanically responsive motion of microchannel-programmed actuators. *Adv. Mater.* **29**, 1702231 (2017).
37. T. F. Fan *et al*., Transformation of hard pollen into soft matter. *Nat. Commun.* **11**, 1449 (2020).
38. Z. Zhao *et al*., Actuation and locomotion driven by moisture in paper made with natural pollen. *Proc. Natl. Acad. Sci. U.S.A.* **117**, 8711–8718 (2020).
39. C. Zhao, Q. Liu, L. Ren, Z. Song, J. Wang, A 3D micromechanical study of hygroscopic coiling deformation in *Pelargonium* seed: From material and mechanics perspective. *J. Mater. Sci.* **52**, 415–430 (2016).
40. E. T. S. G. da Silva, T. M. R. Alves, L. T. Kubota, Direct toner printing: A versatile technology for easy fabrication of flexible miniaturized electrodes. *Electroanalysis* **30**, 345–352 (2018).
41. C. Dawson, J. F. V. Vincent, A.-M. Rocca, How pine cones open. *Nature* **390**, 668 (1997).
42. R. Elbaum, L. Zaltzman, I. Burgert, P. Fratzl, The role of wheat awns in the seed dispersal unit. *Science* **316**, 884–886 (2007).
43. S. Armon, E. Efrati, R. Kupferman, E. Sharon, Geometry and mechanics in the opening of chiral seed pods. *Science* **333**, 1726–1730 (2011).
44. E. Reyssat, L. Mahadevan, Hygromorphs: From pine cones to biomimetic bilayers. *J. R. Soc. Interface* **6**, 951–957 (2009).
45. J. S. Day, Anatomy of capsule dehiscence in sesame varieties. *J. Agric. Sci.* **134**, 45–53 (2000).
46. Y. Abraham, R. Elbaum, Hygroscopic movements in Geraniaceae: The structural variations that are responsible for coiling or bending. *New Phytol.* **199**, 584–594 (2013).
47. Y. Abraham *et al*., Tilted cellulose arrangement as a novel mechanism for hygroscopic coiling in the stork's bill awn. *J. R. Soc. Interface* **9**, 640–647 (2012).
48. L. B. Freund, S. Suresh, *Thin Film Materials: Stress, Defect Formation and Surface Evolution* (Cambridge University Press, 2004).
49. Y. Shen, S. Suresh, I. Blech, Stresses, curvatures, and shape changes arising from patterned lines on silicon wafers. *J. Appl. Phys.* **80**, 1388–1398 (1996).
50. J. H. W. Haslach, The moisture and rate-dependent mechanical properties of paper: A review. *Mech. Time Depend. Mater.* **4**, 169–210 (2000).
51. A. M. Abdullah, K. Nan, J. A. Rogers, K. J. Hsia, Mismatch strain programmed shape transformation of curved bilayer-flexible support assembly. *Extreme Mech. Lett.* **7**, 34–41 (2016).
52. H. Hu, C. Huang, X. H. Liu, K. J. Hsia, Thin film wrinkling by strain mismatch on 3D surfaces. *Extreme Mech. Lett.* **8**, 107–113 (2016).
53. A. M. Abdullah, X. Li, P. V. Braun, J. A. Rogers, K. J. Hsia, Self-folded gripper-like architectures from stimuli-responsive bilayers. *Adv. Mater.* **30**, e1801669 (2018).
54. Hewlett-Packard, "Safety data sheet of HP LaserJet CF276A-X-XC print cartridge" (Hewlett-Packard, Boise, ID, 2020).
55. Dassault Systèmes, "ABAQUS documentation" (Dassault Systèmes, Providence, RI, 2014).
56. Burleigh Park Orchids, The antelope orchids. http://www.speciesorchids.com/CeretobeDendrobiums.html. Accessed 5 October 2020.